Am J Transl Res 2026;18(5):4265-4279
www.ajtr.org /ISSN:1943-8141/AJTR0172305

Original Article

Cross-linked (R)-(+)-lipoic acid nanoparticles loaded with silibinin induce apoptosis and autophagy in glioblastoma cells

Xin Dai[1], Lin Liu[2], Nana Guo[2], Chaokun Mao[3], Xuesen Yan[3]

[1]Department of Basic Teaching, Zunyi Medical and Pharmaceutical College, Zunyi 563006, Guizhou, China; [2]School of Pharmacy, Zunyi Medical University, Zunyi 563000, Guizhou, China; [3]Department of Medical Technology, Zunyi Medical and Pharmaceutical College, Zunyi 563006, Guizhou, China

Received February 26, 2026; Accepted April 19, 2026; Epub May 15, 2026; Published May 30, 2026

Abstract: Objective: To overcome the limitations of poor water solubility and suboptimal tumour-targeting efficiency of silibinin (SF), this study aimed to develop a novel (R)-(+)-lipoic acid (LA)-derived nanocarrier platform to enhance its delivery efficiency and to investigate its antitumor effects and underlying mechanisms in glioblastoma. Methods: Silibinin-loaded (R)-(+)-lipoic acid nanoparticles (SF@LA-NPs) were prepared by a self-assembly approach combined with ultraviolet light-induced crosslinking. Their physicochemical properties, drug encapsulation efficiency, and glutathione (GSH)-responsive release were systematically characterized. Human glioblastoma U87-MG cells were used to evaluate the anti-glioblastoma effects and underlying mechanisms through cytotoxicity assays, intracellular uptake analysis, apoptosis/autophagy analysis, and exploration of the interplay between autophagy and apoptosis. Results: SF@LA-NPs exhibited uniform particle sizes, high drug encapsulation, and rapid GSH-responsive cargo release. Compared to free SF, SF@LA-NPs markedly enhanced intracellular uptake and cytotoxicity. SF@LA-NPs induced overproduction of reactive oxygen species (ROS), leading to mitochondrial damage and activation of the Caspase-3-dependent apoptosis pathway. Notably, SF@LA-NPs concurrently triggered a protective autophagic response, as indicated by increased LC3-II conversion and reduced p62. In addition, a functional antagonistic relationship was uncovered: pharmacologic inhibition of autophagy enhanced apoptosis and cytotoxicity, while inhibition of apoptosis attenuated cell death and altered autophagic activity. Conclusion: SF@LA-NPs developed in this study significantly enhanced the delivery efficiency and antitumor activity of silibinin in glioblastoma cells. Moreover, a dual-mechanism mode of action was elucidated, involving ROS-induced mitochondrial apoptosis and compensatory protective autophagy. These findings provide a promising nano-platform and a theoretical basis for combination therapies targeting apoptosis-autophagy crosstalk in glioblastoma.

Keywords: Glioblastoma, silibinin, (R)-(+)-lipoic acid, apoptosis, autophagy

Introduction

Glioblastoma is the most invasive primary malignant tumor of the central nervous system, and its treatment remains highly challenging due to the presence of the blood-brain barrier (BBB), pronounced tumor heterogeneity, and susceptibility to drug resistance. The five-year survival rate of patients is only about 5% [1-4]. Silibinin is a flavonolignan complex extracted from the seeds of Silybum marianum, exhibiting antioxidant, anti-inflammatory, and significant anti-tumor activities [5, 6]. Research has shown that it can induce cell cycle arrest and promote apoptosis as well as autophagic cell death in various cancer cell lines, including glioblastoma, through the regulation of multiple signaling pathways [7-9]. However, its poor water solubility, low oral bioavailability, rapid systemic clearance, and limited ability to penetrate the BBB severely limit its clinical application [10, 11]. Therefore, there is an urgent need to develop new delivery strategies that can overcome the aforementioned obstacles.

Nanoparticle-mediated drug delivery systems provide a promising strategy to address these obstacles. Encapsulation of drugs within nano-

https://doi.org/10.62347/BINO1467

carriers can significantly improve the solubility of hydrophobic drugs, extend systemic circulation time, and facilitate passive tumor targeting through the enhanced permeability and retention (EPR) effect observed in solid tumors [12]. In addition, surface functionalization of nanocarriers (such as conjugation with targeting peptides or antibodies) enables active targeting through specific interactions with receptors that are overexpressed on tumor cells or tumor-associated vasculature [13].

Among various nanomaterials, stimuli-responsive and biodegradable nanocarriers have attracted considerable attention due to their ability to achieve controlled drug release in response to specific triggers from the tumor microenvironment, such as acidic pH or elevated intracellular glutathione (GSH) levels [14, 15]. In this context, (R)-(+)-lipoic acid (LA), as an endogenous co-factor with high biocompatibility, also exhibits certain advantages. Its molecular structure contains a disulfide bond, which can form stable three-dimensional nanostructures through mild oxidation or photopolymerization. This disulfide bond can be selectively cleaved by the elevated levels of GSH within cancer cells, enabling redox-responsive drug release [16, 17]. Unlike conventional "passive" carrier materials, such as poly (lactic-co-glycolic acid) (PLGA), LA and its metabolic derivatives retain intrinsic biological functions, including antioxidant effects and regulation of cellular energy metabolism. These properties suggest potential synergistic anticancer effects with the encapsulated drug, supporting the new concept of "medicine as the vehicle" [18]. Indeed, previous studies have reported that cross-linked vesicles prepared solely of LA exhibit significant synergistic anti-cancer efficacy [19].

Although nano-carrier technology shows great potential, it remains challenging to construct an integrated nanoplatform capable of achieving high drug loading, tumor microenvironment-responsive release, and simultaneous activation of multiple programmed cell death pathways, including apoptosis and autophagy. Based on this, this study aims to build an intelligent delivery system based on LA for the efficient delivery of SF and to explore its therapeutic potential in glioblastoma.

Materials and methods

Reagents and materials

(R)-(+)-Lipoic acid (LA) and silibinin (SF), with purities of > 99% and 98%, respectively, were obtained from Shanghai Macklin Biochemical Technology Co., Ltd. (Shanghai, China). Coumarin-6 and reduced GSH were sourced from Sigma-Aldrich (St. Louis, MO, USA). Fetal Bovine Serum (FBS), DMEM high-glucose medium, 0.25% trypsin-EDTA solution, and penicillin-streptomycin solution (P/S) were purchased from Gibco (Grand Island, NY, USA).

Cell Counting Kit-8 (CCK-8) and Annexin V-FITC/PI apoptosis detection kits were purchased from Dojindo Molecular Technologies (Kumamoto, Japan). The ROS assay kit (DCFH-DA, Cat# S0033S) and JC-1 mitochondrial membrane potential assay kit (Cat# C2006) were obtained from Beyotime Biotechnology (Shanghai, China).

Antibodies used for Western blotting included rabbit monoclonal anti-cleaved Caspase-3 (Cat# 9664, 1:1000), anti-Cleaved PARP (Cat# 5625, 1:1000), anti-LC3B (Cat# 3868, 1:1000), anti-p62/SQSTM1 (Cat# 8025, 1:1000), anti-p-mTOR (Cat# 5536, 1:1000), anti-mTOR (Cat# 2983, 1:1000), anti-Bax (Cat# 5023, 1:1000), anti-Bcl-2 (Cat# 4223, 1:1000), anti-Cytochrome c (Cat# 4280, 1:1000), and mouse monoclonal anti-GAPDH (Cat# 5174, 1:5000), and HRP-conjugated goat anti-rabbit (Cat# 7074, 1:2000) and anti-mouse (Cat# 7076, 1:2000) secondary antibodies. All antibodies were purchased from Cell Signaling Technology (Danvers, MA, USA).

DAPI (nuclear staining dye) and the autophagy inhibitor 3-methyladenine (3-MA) were purchased from Beyotime Biotechnology (Shanghai, China). Acetonitrile and methanol (HPLC grade) were used for high-performance liquid chromatography (HPLC) analysis. Other reagents, including acetone and dimethyl sulfoxide (DMSO), were also of analytical grade and purchased from Sinopharm Chemical Reagent Co., Ltd. (Shanghai, China). Ultrapure water with a resistivity of 18.2 MΩ·cm was used throughout all experiments.

The human glioblastoma cell line U87-MG was obtained from American Type Culture Collection (ATCC, Manassas, VA, USA). Cells were cultured in a humidified incubator at 37°C under 5% CO_2.

Preparation of SF@LA-NPs

Silibinin-encapsulated cross-linked (R)-(+)-lipoic acid nanoparticles (SF@LA-NPs) were synthesized utilizing a nanoprecipitation method combined with ultraviolet (UV)-induced cross-linking [20, 21]. Specifically, LA (82.5 mg) and SF (17.5 mg) were dissolved in 4 mL of acetone to form a homogeneous organic phase. This organic mixture was subsequently added dropwise (1 mL/min) into 40 mL of ultrapure water under vigorous magnetic stirring. After complete addition, the mixture was continuously stirred for an additional 30 min. Subsequently, the dispersion was transferred to a fume hood, and acetone was carefully evaporated by nitrogen purging for 4 h. The resulting nanoparticle suspension was then kept at 4°C overnight to allow structural stabilization. Thereafter, the dispersion was transferred into a quartz tube and irradiated with 365 nm UV light for 4 h to induce disulfide bond-mediated crosslinking between LA molecules. Ultimately, the cross-linked nanoparticles were purified by dialysis (molecular weight cutoff: 1 kDa) against ultrapure water at 4°C for 48 h. The obtained SF@LA-NPs were preserved at 4°C in the dark for subsequent application. Blank nanoparticles (LA-NPs) were synthesized following the same protocol without the addition of SF. Free SF solution was prepared by dissolving SF in DMSO to obtain a 50 mM stock solution, followed by dilution with complete culture medium to the required working concentrations. The final concentration of DMSO in all treatment groups was maintained below 0.1% (v/v). The physicochemical properties of SF@LA-NPs were characterized by dynamic light scattering (DLS) and transmission electron microscopy (TEM).

Fourier transform infrared (FTIR) spectroscopy

To verify the formation of disulfide bonds and successful drug encapsulation, Fourier transform infrared (FTIR) spectroscopy was performed on unmodified LA particles, freeze-dried LA-NPs, and SF@LA-NPs. Each sample was thoroughly mixed with potassium bromide (KBr), ground into a fine powder, and compressed into transparent pellets for measurement. Spectra were recorded over a wavenumber range of 4000-400 cm^{-1}, with a resolution of 4 cm^{-1}.

Determination of drug encapsulation efficiency and drug loading content

The encapsulation efficiency (EE) and drug loading (DL) of SF were quantified using HPLC. A standard calibration curve was established using SF reference solutions prepared in methanol at concentrations ranging from 1 to 100 μg/mL. Chromatographic separation was performed on a C18 column using a mobile phase consisting of acetonitrile and 0.1% formic acid in water (55:45, v/v) at a flow rate of 1.0 mL/min. The analytical wavelength was set to 288 nm.

To determine the total drug load (W_{total}), 1.0 mL of SF@LA-NPs dispersion was mixed with 9.0 mL of methanol, followed by vigorous vortexing and ultrasonication for 10 min to ensure complete nanoparticle disruption and drug release. Subsequently, the obtained solution was filtered through a 0.22 μm microporous membrane, and the SF concentration in the filtrate was determined by HPLC.

To quantify the unencapsulated drug (W_{free}), 1.0 mL of the SF@LA-NPs dispersion was added to an ultrafiltration centrifugal tube (molecular weight cut-off: 1 kDa) and centrifuged at 14,000×g for 20 min. The concentration of SF in the filtrate was determined using HPLC.

The total mass of nanoparticles ($W_{nanoparticles}$) was determined by lyophilising a certain volume of nanoparticle dispersion and weighing the resulting solid precipitate. The encapsulation efficiency (EE, %) and drug loading (DL, %) were calculated according to the follow-ing equations: $EE (\%) = [(W_{total} - W_{free})/W_{total}] \times 100\%$; $DL (\%) = [(W_{total} - W_{free})/W_{nanoparticles}] \times 100\%$.

In vitro release assay

1 mL of SF@LA-NPs suspension was sealed in a dialysis bag (molecular weight cutoff: 1 kDa), which was then immersed in 50 mL of distinct release media: PBS (pH 7.4), PBS supplemented with 10 mM GSH, and acetate buffer (pH 5.5). The system was maintained in a thermostatic shaker at 37°C with a shaking speed of 100 rpm. At predetermined time points, the external release medium was withdrawn and immediately replaced with an equal volume of fresh prewarmed medium to maintain sink con-

ditions. The collected samples were analyzed by HPLC to quantify the released SF, and cumulative release profiles were calculated. As a control, an equivalent quantity of free SF, originally dissolved in a small volume of DMSO, was diluted in PBS and subjected to the same release protocol.

Storage stability study

The physical stability of SF@LA-NPs was evaluated over time. The nanoparticle suspension was stored at 4°C in the dark. At the specified time points (0, 5, 10, 15, 20, 30 days), samples were collected, and their hydrodynamic diameter and PDI were determined by DLS using the standard procedure mentioned above.

Cell culture

The human glioblastoma cell line U87-MG was cultured in standard conditions using Dulbecco's Modified Eagle Medium (DMEM) supplemented with 10% (v/v) FBS and 1% (v/v) P/S. Cells were maintained in a humidified incubator at 37°C with 5% CO_2. Cells in the logarithmic growth phase were used for all experiments.

Cell viability assay

U87-MG cells were inoculated into a 96-well plate at a density of 5×10^3 cells per well and cultured for 24 h to allow cell attachment. The cells were subsequently distributed into various treatment groups: including control (culture medium only), free SF, blank LA nanoparticles (LA-NPs), SF-loaded LA nanoparticles (SF@LA-NPs), and temozolomide (TMZ) as a positive control. For drug treatment groups, a series of concentrations was applied. Free SF and SF@LA-NPs were tested at equivalent SF concentrations (12.5, 25, 50, 100, 150, 200, and 300 μM). The concentration of blank LA-NPs was adjusted to match the total nanoparticle mass in the corresponding SF@LA-NPs groups. Cells were incubated with 100 μL of fresh medium supplemented with the relevant treatment agents for 24 or 48 h. Subsequently, 10 μL of CCK-8 reagent was introduced into each well, followed by incubation for an extra 2 h. The absorbance at 450 nm was measured using a microplate reader (BioTek Synergy H1, USA), and the cell viability was calculated accordingly.

Cellular uptake

Coumarin-6 was used as a fluorescent probe to replace SF, and fluorescently labeled nanoparticles (Cou-6@LA-NPs) were prepared using the same procedure described above. U87-MG cells were seeded in confocal microscopy dishes and allowed to adhere. These cells were incubated with medium containing either free Coumarin-6 or Cou-6@LA-NPs for 2 and 4 h. After treatment, the cells were rinsed three times with PBS, fixed with 4% paraformaldehyde for 15 min, and subsequently stained with DAPI for 10 min to visualize nuclei. These samples were observed and collected using a laser scanning confocal microscope. For quantitative analysis by flow cytometry, cells were treated under the same conditions, followed by trypsinization, washing with PBS, and re-suspension. The fluorescence intensity of the cells was measured using flow cytometry, and then the mean fluorescence intensity (MFI) was calculated.

Apoptosis assay

Cell apoptosis was assessed using the Annexin V-FITC/PI apoptosis detection kit. U87-MG cells were seeded into 6-well plates at a density of 5×10^5 per well and incubated for 24 h. Cells were then treated with the indicated formulations at designated concentrations for an additional 24 h. Subsequently, cells were harvested, washed with PBS, and stained with Annexin V-FITC and PI at room temperature in the dark for 15 min, followed by analysis using flow cytometry.

Measurement of intracellular ROS

Intracellular ROS levels were quantified using the fluorescent probe DCFH-DA. After treatment for 24 h, cells were incubated with 10 μM DCFH-DA in serum-free conditions at 37°C for 30 min. These cells were subsequently rinsed with PBS, and fluorescence intensity was assessed by flow cytometry.

Measurement of mitochondrial membrane potential

Mitochondrial membrane potential was evaluated using the JC-1 staining assay. Following 24 h of incubation, cells were collected and incubated with JC-1 staining solution at 37°C for 20 min according to the manufacturer's instructions. The fluorescence signal was analyzed by flow cytometry. A reduction in the red/green fluorescence intensity ratio suggests mitochondrial membrane depolarization.

Functional crosstalk between apoptosis and autophagy

To investigate the interaction between programmed cell death and autophagy, the following groups were established: Control, Free SF, SF@LA-NPs, SF@LA-NPs + 3-MA, SF@LA-NPs + Z-VAD-FMK. For inhibitor treatment groups, cells were pretreated with 5 mM 3-MA or 20 μM Z-VAD-FMK for 1 h. Subsequently, the culture medium was replaced with fresh medium containing SF@LA-NPs while maintaining the respective inhibitor concentrations. These cells were then incubated for 12 h (for western blotting and immunofluorescence experiments) or 24 h (for cell viability and apoptosis assays).

Immunofluorescence

Cells were fixed, permeabilized, and blocked. Subsequently, cells were incubated with a primary antibody targeting LC3 overnight at 4°C, followed by incubation with an FITC-labeled secondary antibody at room temperature for 1 h. Nuclei were counterstained with DAPI. Fluorescence images were acquired using a laser scanning confocal microscope. LC3-positive puncta, representing autophagosomes, were quantified for semi-quantitative evaluation.

Western blot analysis

Following treatment, cells were washed three times with PBS and lysed in RIPA buffer for total protein extraction. Protein concentrations were measured using the BCA method. Equal amounts of protein were separated by SDS-PAGE and subsequently transferred onto PVDF membranes (Millipore). These membranes were blocked with 5% non-fat milk for 1 h at room temperature and then incubated overnight at 4°C with primary antibodies against cleaved Caspase-3, cleaved PARP, p-mTOR, mTOR, Bax, Bcl-2, Cyt-c, LC3-I, LC3-II, p62 and β-actin or GAPDH. After washing, the membranes were incubated with HRP-labeled secondary antibodies at room temperature for 1 h. Protein bands were visualized using ECL reagents, and band intensities were quantified using Image J software.

Statistical analysis

Data were presented as mean ± standard deviation (SD) from at least three independent experiments ($n \geq 3$). Statistical analyses were performed using GraphPad Prism 9.0 software. For comparisons between two groups, an unpaired two-tailed Student's t-test was used. For comparisons among multiple groups, one-way analysis of variance (ANOVA) followed by Tukey's post hoc test was applied. For comparisons involving multiple factors, two-way ANOVA followed by Šidák's post hoc test was used. A *P*-value < 0.05 was regarded as statistically significant. Significance was denoted as follows: ns, not significant; *$P < 0.05$; **$P < 0.01$; ***$P < 0.001$; ****$P < 0.0001$.

Results

Preparation, characterization, and in vitro evaluation of SF@LA-NPs

SF@LA-NPs were successfully prepared using a nanoprecipitation method combined with UV light-mediated crosslinking. The physicochemical properties of these nanoparticles were systematically characterized. DLS tests showed that the hydrodynamic diameters of blank LA-NPs and SF@LA-NPs were 78.1 ± 1.3 nm and 107.8 ± 2.0 nm, respectively, with PDI < 0.20, indicating a uniform size distribution (**Figure 1A**). The increase in particle size after drug loading indicates successful encapsulation of SF. Both formulations exhibited negative zeta potentials; specifically, LA-NPs had a value of -22.3 ± 0.4 mV, while SF@LA-NPs showed a value of -19.5 ± 1.2 mV (**Figure 1B**), with slight surface charge variation after drug incorporation. TEM images revealed that SF@LA-NPs were spherical in morphology, well-dispersed, and free of obvious aggregation, which was consistent with the DLS results (**Figure 1C**).

FTIR spectroscopy further confirmed the structural characteristics and successful drug encapsulation. As shown in **Figure 1D**, free LA showed a characteristic thiol (-S-H) stretching vibration peak at approximately 2550 cm^{-1}. The peak disappeared in both LA-NPs and SF@LA-NPs, indicating the formation of disulfide (-S-S-) bonds between LA molecules upon

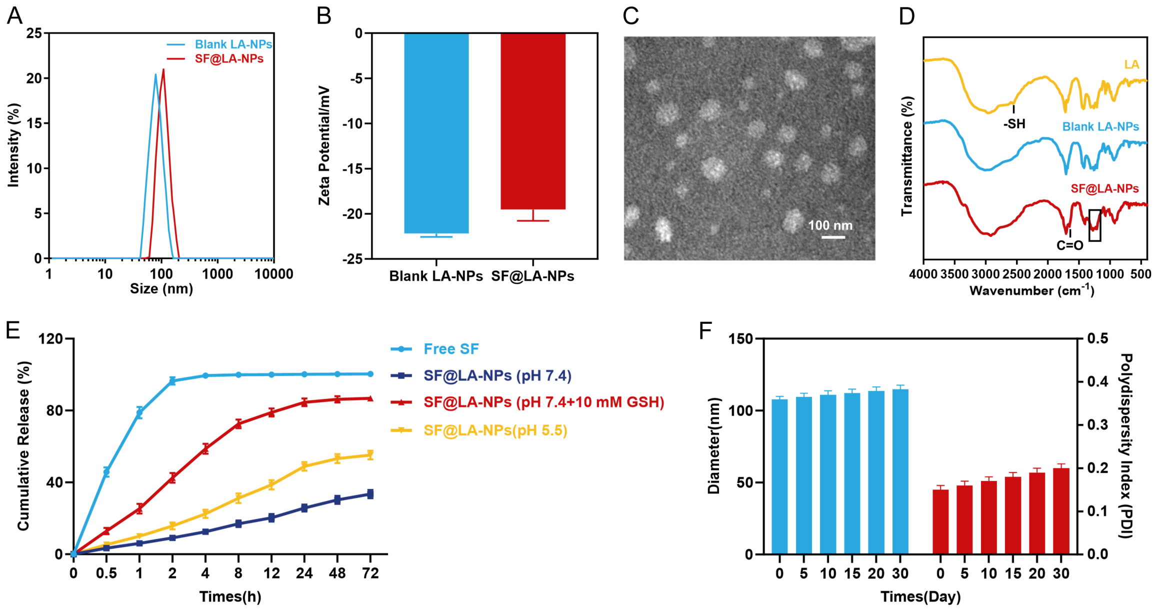

Figure 1. Synthesis, characterization, and *in vitro* assessment of SF@LA-NPs. (A) Particle size and PDI values of LA-NPs and SF@LA-NPs. (B) Zeta potential for LA-NPs and SF@LA-NPs. (C) Transmission electron microscopy image of SF@LA-NPs; Scale bar: 100 nm. (D) FTIR analysis of free LA, blank LA-NPs, and SF@LA-NPs. (E) In vitro cumulative release patterns of SF@LA-NPs across various release media. (F) Evolution of particle size and PDI in SF@LA-NPs suspensions over 30 days of storage at 4°C in darkness.

UV irradiation. In addition, specific absorption peaks of SF, including the C = O stretching vibration at approximately 1650 cm^{-1} and aromatic ring vibrations near 1200 cm^{-1}, were retained in the spectrum of SF@LA-NPs, confirming successful drug incorporation. The drug-loading capacity was further evaluated using HPLC. The results showed that SF@LA-NPs achieved an encapsulation efficiency (EE) of 85.4 ± 1.7% and a drug loading (DL) of 14.9 ± 0.4%, indicating efficient drug incorporation.

The drug release behavior and stability of the nanosystem were evaluated. As shown in **Figure 1E**, SF@LA-NPs exhibited sustained release under physiological conditions (pH 7.4), with a cumulative release of 33.5 ± 2.35% over 72 h, indicating good stability in the blood circulation. In reductive environment containing 10 mM GSH, mimicking the intracellular tumor milieu, drug release was significantly accelerated, reaching 84.6 ± 2.1% within 24 h, followed by a plateau phase. This indicates excellent redox-responsive release behavior. Under a mildly acidic environment (pH 5.5), the release rate was slightly increased compared with physiological conditions (72 h cumulative release rate: 55.2 ± 2.4%), indicating limited pH responsiveness relative to GSH sensitivity. In contrast, free SF was rapidly released within a few hours.

The physical stability of the formulation was further investigated. As illustrated in **Figure 1F**, SF@LA-NPs stored at 4°C in the dark exhibited minimal changes over 30 days. The mean particle size increased slightly from 107.8 nm to 114.9 nm, whereas the PDI remained below 0.20 throughout the storage period. These results indicate that the nanosystem exhibits excellent physical stability and is suitable for short-term storage.

In vitro antitumor activity and enhanced cellular uptake of SF@LA-NPs

The growth-suppressing effects of SF@LA-NPs against U87-MG cells were evaluated using the CCK-8 assay. As illustrated in **Figure 2A**, blank LA-NPs exhibited negligible cytotoxicity, with cell viability > 90% throughout the experimental concentration range, indicating good biocompatibility of the nanocarrier system. Both free SF and SF@LA-NPs suppressed cell proliferation in a dose- and time-dependent pattern; nevertheless, SF@LA-NPs demonstrated notably enhanced cytotoxic effects com-

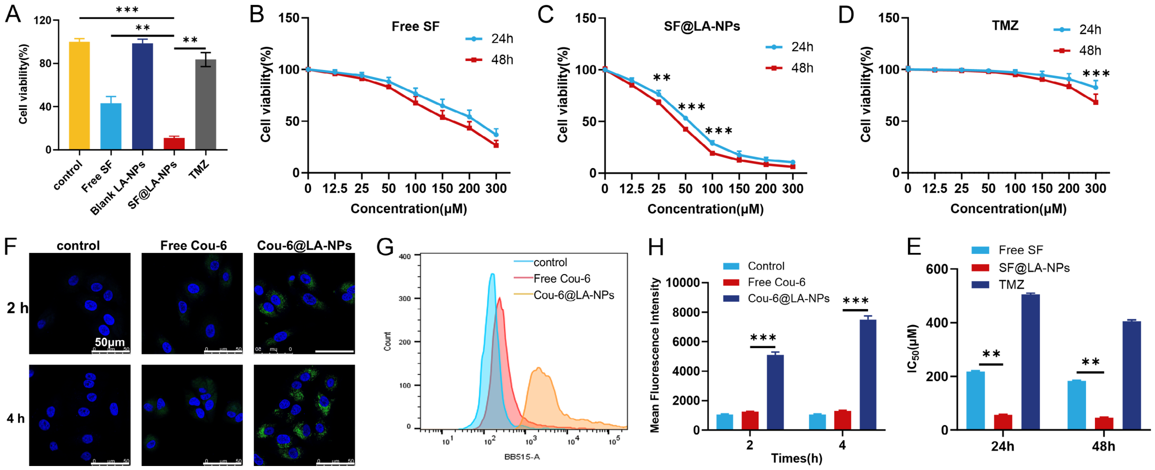

Figure 2. *In vitro* antitumor activity and enhanced cellular uptake of SF@LA-NPs. (A) Cell viability of U87-MG cells after 48 h treatment with a typical dosage (200 μM SF equivalent) across different groups. (B-D) Dose-response curves of U87-MG cells incubated with free SF, SF@LA-NPs, and TMZ for 24 h and 48 h. (E) Calculated IC_{50} for free SF, SF@LA-NPs, and TMZ at 24 h and 48 h, derived from the dose-response curves. (F) Confocal laser scanning microscope images demonstrating cellular uptake of Cou-6 and Cou-6@LA-NPs in U87-MG cells after 2 h and 4 h incubation. Green: Cou-6; Blue: DAPI-labeled nuclei. Scale bar: 50 μm. (G, H) Flow cytometry analysis of mean fluorescence intensity in U87-MG cells following 4 h incubation. $^{**}P < 0.01$, $^{***}P < 0.001$.

pared with free SF (**Figure 2B-D**). The half-maximal inhibitory concentration (IC_{50}) values of SF@LA-NPs were 56 ± 2.2 μM and 46 ± 1.9 μM at 24 h and 48 h, respectively, which were notably lower than those for free SF under identical conditions (218 ± 6.5 μM at 24 h and 182 ± 5.8 μM at 48 h) (**Figure 2E**), further supporting above observation. The IC_{50} value of the clinically used therapeutic drug, temozolomide (TMZ), was 405 ± 10.5 μM at 48 h. These findings indicate that the nano-encapsulation system markedly improved the cytotoxicity of SF against U87-MG cells, with greater efficacy than TMZ under the tested conditions.

To explore the underlying mechanism of this enhanced effect, cellular uptake efficiency was evaluated. Confocal laser scanning microscopy (CLSM) images (**Figure 2F**) revealed strong intracellular green fluorescent signals in cells incubated with Cou-6@LA-NPs after 2 h and 4 h, whereas only weak and scattered fluorescence was observed in cells treated with free Coumarin-6 (Cou-6). Moreover, fluorescence intensity increased over time, indicating efficient cellular internalization and sustained intracellular accumulation of the nanoparticles. Flow cytometric analysis further confirmed this result (**Figure 2G**, **2H**). Following 4 h of incubation, the MFI of cells treated with Cou-6@LA-NPs (8500 ± 250 a.u.) was roughly 6.5-fold higher than that of the free Cou-6 group (1300 ± 50 a.u.) ($P < 0.001$). These results demonstrate that LA-NPs significantly enhance intracellular delivery efficiency, contributing to the improved antitumor activity observed.

SF@LA-NPs induced cell apoptosis

As illustrated in **Figure 3A**, **3B**, following 24-h incubation at an equivalent SF dose of 50 μM, the apoptotic rates in both the control group and blank LA-NPs group remained below 5%. Free SF treatment induced apoptosis in 19.8 ± 2.15% of cells. Conversely, SF@LA-NPs at the same concentration significantly increased the total apoptotic rate to 57.63 ± 3.65%, predominantly in early phase. This pro-apoptotic effect was markedly greater than that of free SF ($P < 0.001$).

Western blot analysis further confirmed activation of the apoptotic signaling pathway in U87-MG cells (**Figure 3C**, **3D**). Compared with the control group, SF@LA-NPs significantly increased the protein expression of cleaved caspase-3 and its downstream target cleaved PARP. The expression levels were approximately 2.17-fold and 2.2-fold higher, respectively, than those observed in the free SF group ($P < 0.01$). In contrast, free SF induced only modest changes in these proteins, while blank LA-NPs

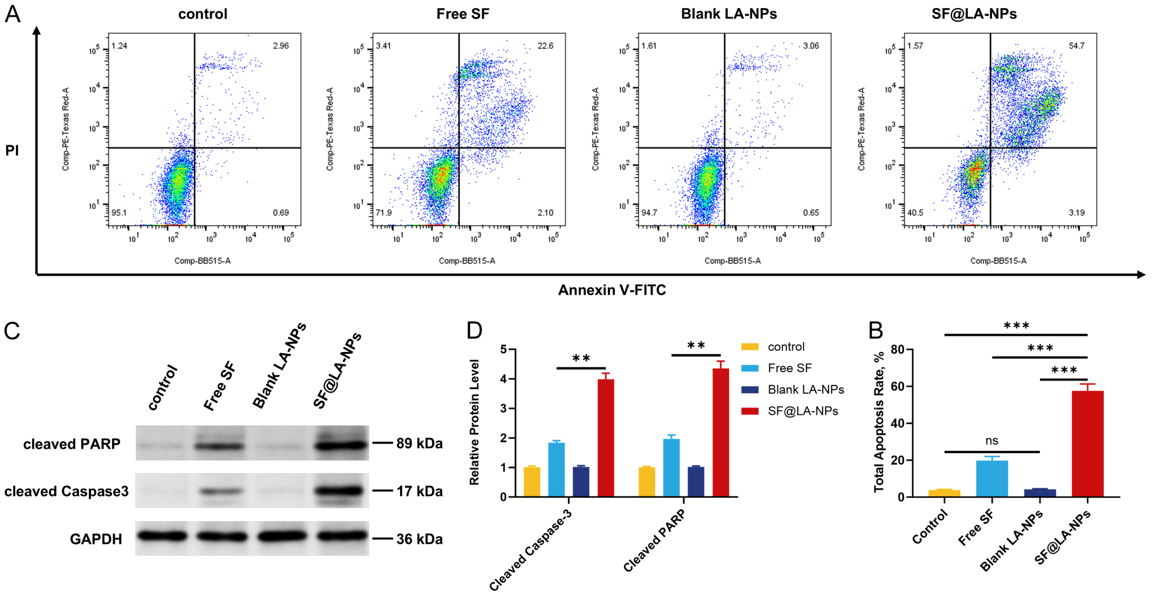

Figure 3. SF@LA-NPs induced apoptosis in U87-MG cells. (A, B) Representative flow cytometry dot plots and quantitative analysis of apoptosis in different groups, determined by Annexin V-FITC/PI dual staining. (C, D) Western blot analysis of apoptosis-related markers, including cleaved Caspase-3 and cleaved PARP, along with the corresponding semi-quantitative analysis. $^{**}P < 0.01$, $^{***}P < 0.001$.

exhibited no significant effect. These results indicate that SF@LA-NPs effectively induce apoptosis in U87-MG cells via activation of the conventional Caspase-3/PARP-dependent pathway.

SF@LA-NPs induced ROS-mediated mitochondrial apoptosis

To elucidate the upstream mechanisms underlying SF@LA-NPs-induced cytotoxicity, intracellular ROS production and mitochondrial apoptotic signaling were investigated. As shown in **Figure 4A**, **4B**, treatment with SF@LA-NPs significantly increased intracellular ROS levels in U87-MG cells compared with free SF and blank nanoparticles, reaching approximately 4.2-fold higher than the control group. This phenomenon was significantly alleviated by the ROS scavenger N-acetylcysteine ($P < 0.001$), indicating that SF@LA-NPs induced pronounced oxidative stress.

Excessive ROS generation was accompanied by substantial mitochondrial dysfunction. JC-1 staining (**Figure 4C**, **4D**) showed a significant decrease in mitochondrial membrane potential following SF@LA-NPs treatment, which was partially reversed by NAC ($P < 0.01$), indicating that ROS-mediated oxidative stress contributes to mitochondrial damage.

From a molecular perspective, western blot analysis also confirmed the involvement of the mitochondrial apoptotic pathway (**Figure 4E-I**). SF@LA-NPs increased the expression of the pro-apoptotic protein Bax while downregulating the anti-apoptotic protein Bcl-2, thereby significantly increasing the Bax/Bcl-2 ratio. In addition, enhanced release of cytochrome c into the cytosol was observed. Such changes were largely attenuated by NAC treatment, suggesting that ROS acts upstream in this signaling cascade.

Functional rescue experiments further verified this mechanism (**Figure 4J**). NAC pretreatment partially reduced SF@LA-NPs-induced cytotoxicity and restored cell viability to 68.0%. Moreover, pan-caspase inhibitor Z-VAD-FMK further increased cell survival. Collectively, these results indicate that SF@LA-NPs induce mitochondrial apoptosis through ROS overproduction, ultimately leading to cell death.

SF@LA-NPs induced protective autophagy and its functional role

We further examined the role of autophagy in the anticancer effects of SF@LA-NPs. Western blot analysis (**Figure 5A**, **5B**) indicated that treatment with SF@LA-NPs for 12 h notably increased the LC3-II/LC3-I ratio while markedly

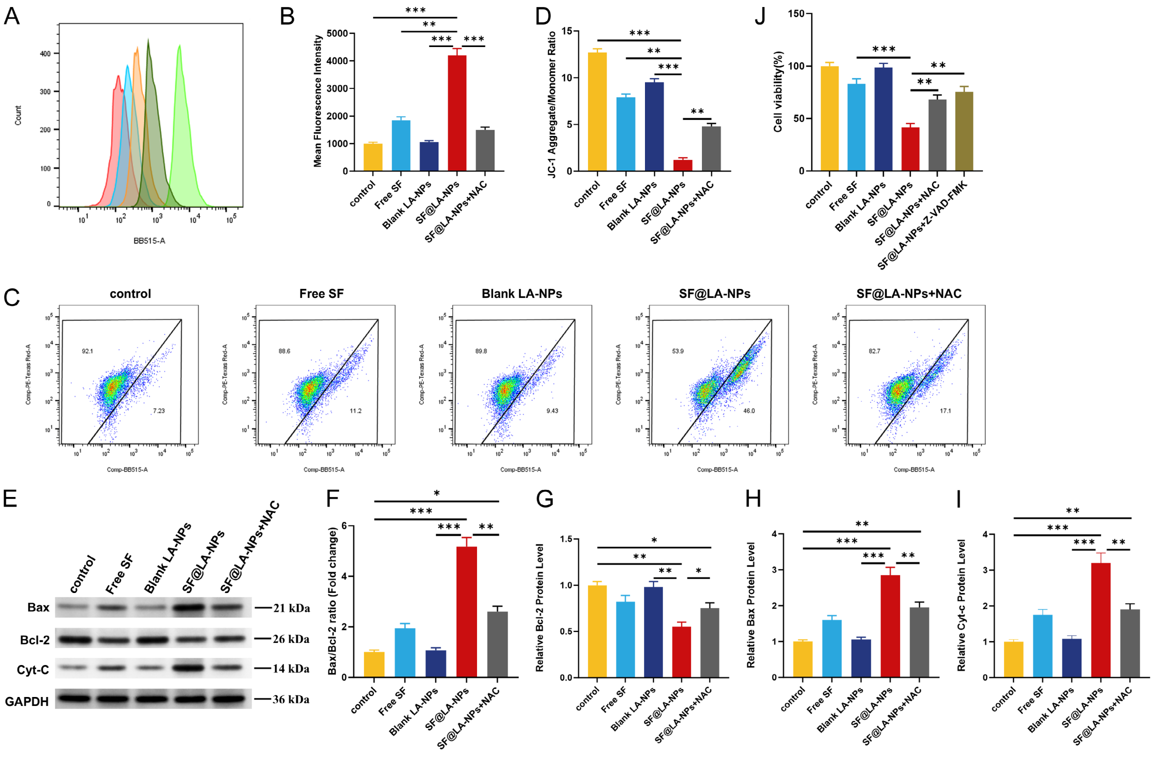

Figure 4. SF@LA-NPs induced apoptosis through the ROS-mediated mitochondrial pathway in U87-MG cells. (A, B) Intracellular ROS levels measured by flow cytometry and the DCFH-DA reagent. (C, D) Changes in mitochondrial membrane potential detected by JC-1 staining. (E) Typical Western blot analysis of apoptosis-related proteins, including Bax, Bcl-2, Cyt-c, and GAPDH. (F-I) Semi-quantitative analysis of Bax/Bcl-2 ratio (F), Bcl-2 protein level (G), Bax protein level (H), and cytosolic Cyt-c protein level (I) relative to the control group. (J) Cell viability recovery experiment evaluated by CCK-8. *$P < 0.05$, **$P < 0.01$, ***$P < 0.001$.

decreasing the protein expression of the autophagic substrate p62 in U87-MG cells. Notably, these changes were more pronounced compared to those observed in the positive control group treated with the autophagy stimulator rapamycin. Conversely, free SF induced only modest alterations in autophagy-related markers. These findings collectively indicate that SF@LA-NPs effectively activate autophagic flux.

Immunofluorescence analysis further validated these findings (**Figure 5C**, **5D**). A substantial increase in LC3-positive puncta was observed in the cytoplasm of cells treated with SF@LA-NPs, with an average of 45.2 ± 3.3 puncta per cell. This was notably greater than that in the free SF group (12.0 ± 1.5 puncta per cell) and the control group (4.7 ± 0.8 puncta per cell) ($P < 0.001$). To elucidate the functional role of autophagy, the autophagy inhibitor 3-MA was applied. Pretreatment with 3-MA notably suppressed LC3 puncta formation induced by SF@LA-NPs (**Figure 5C**, **5D**). Simultaneously, cell viability assays demonstrated the cytoprotective effect of autophagy (**Figure 5E**). Following 12 h of treatment at the same concentration, cell viability in the SF@LA-NPs group reached 62.3 ± 5.1%. Conversely, inhibition of autophagy by 3-MA significantly decreased cell viability to 48.7 ± 4.8% ($P < 0.05$). These findings suggest that SF@LA-NPs-induced autophagy functions as a protective mechanism in U87-MG cells, and pharmacologic inhibition of autophagy may enhance the cytotoxic potential of SF@LA-NPs, thereby improving therapeutic efficacy.

Interplay between apoptosis and autophagy induced by SF@LA-NPs

Given that SF@LA-NPs concurrently induce apoptosis and autophagy, we further examined their association. Western blot analysis (**Figure 6A-E**) demonstrated that inhibition of autophagy using 3-MA not only inhibited autophagic

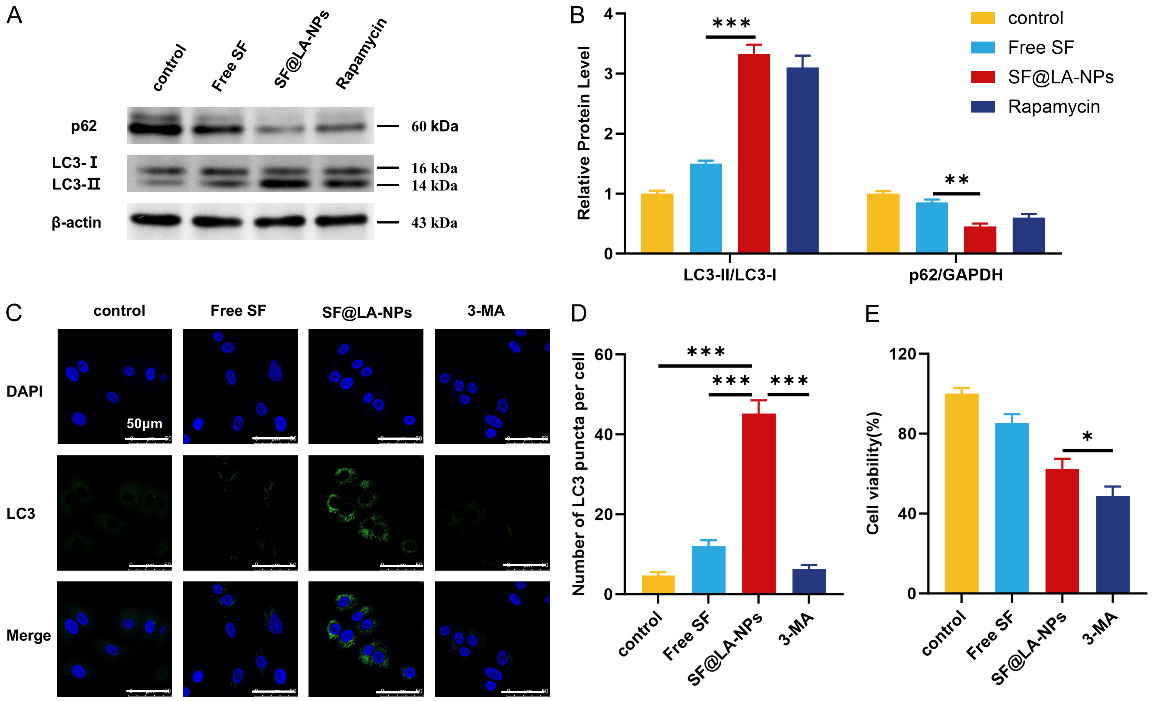

Figure 5. SF@LA-NPs induced cytoprotective autophagy and its functional role in U87-MG cells. (A, B) Western blot analysis of autophagy-related proteins LC3 and p62 (A), along with semi-quantitative analysis of the LC3-II/LC3-I ratio and p62 protein concentration (B). Rapamycin (Rapa) acted as a positive control for autophagy activation. (C, D) Immunofluorescence images showing LC3-positive puncta (green) in U87-MG cells across different groups (C), with quantitative analysis of LC3 puncta per cell (D). Blue: DAPI-stained nuclei. Scale bar: 50 μm. (E) Influence of the autophagy inhibitor 3-MA on the cytotoxicity of SF@LA-NPs. $^{*}P < 0.05$, $^{**}P < 0.01$, $^{***}P < 0.001$.

activity but also significantly increased the expression of the apoptosis-associated protein cleaved Caspase-3. In contrast, inhibition of apoptosis using Z-VAD-FMK significantly reduced the levels of cleaved Caspase-3, while concomitantly increasing the LC3-II/LC3-I ratio and attenuating p62 degradation, indicating enhanced autophagic activity.

This molecular-level antagonism translated into distinct functional outcomes at the cellular level. As illustrated in **Figure 6F-H**, inhibition of autophagy notably potentiated the cytotoxic effects of SF@LA-NPs, resulting in reduced cellular viability and increased apoptosis. Conversely, blocking apoptosis exhibited a protective effect, markedly increasing cell viability (65.0%) and lowering the apoptotic rate (23.6%).

Immunofluorescence analysis provided further visual evidence (**Figure 6I**, **6J**). SF@LA-NPs induced a substantial increase in LC3-positive puncta, indicative of autophagosome formation, which was successfully inhibited by 3-MA. Notably, the number of LC3 puncta in the Z-VAD-FMK co-treatment group remained significantly higher than that in the nanoparticle-only administration group ($P < 0.05$), further confirming the compensatory upregulation of autophagy after apoptosis inhibition.

Discussion

The treatment of glioblastoma remains severely constrained by multiple challenges, including the presence of the blood-brain barrier, tumor heterogeneity, and resistance to TMZ [22-24]. To address these challenges, this study developed and validated an intelligent nano-delivery platform (SF@LA-NPs) based on the endogenous compound (R)-(+)-LA. This system aimed to enhance the delivery efficiency of SF and modulate tumor cell fate, thereby providing a potential therapeutic strategy for glioblastoma.

The key advantage of this platform lies in the unique properties of LA as a carrier. In contrast to the traditional inert polymers such as PLGA,

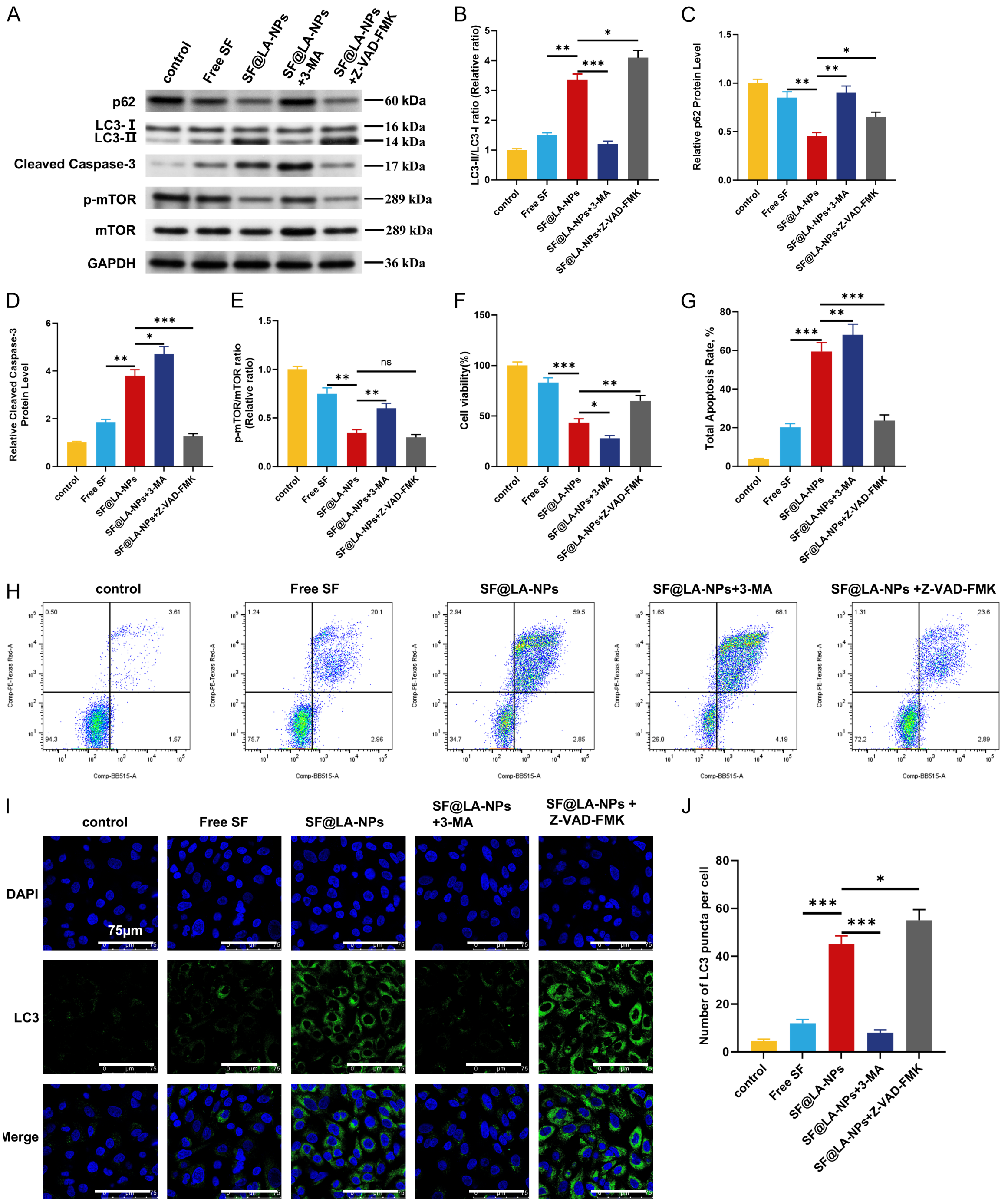

Figure 6. Crosstalk between apoptosis and autophagy induced by SF@LA-NPs in U87-MG cells. (A) Western blot analysis of protein levels of LC3-I/II, p62, cleaved Caspase-3, p-mTOR, mTOR, and GAPDH. (B-E) Semi-quantitative analysis of the LC3-II/LC3-I ratio (B), p62 expression levels (C), cleaved Caspase-3 levels (D), and p-mTOR/mTOR ratio (E). (F) Cell viability determined by CCK-8. (G) Apoptotic rate measured by Annexin V/PI flow cytometry. (H) Characteristic flow cytometric dot plots of apoptosis. (I) Immunofluorescence images showing LC3-positive puncta (green) and DAPI-stained nuclei (blue). Scale bar: 75 μm. (J) Quantitative analysis of LC3 puncta per cell. $^{*}P < 0.05$, $^{**}P < 0.01$, $^{***}P < 0.001$.

LA can form stable and redox-responsive nanoarchitectures through disulfide bond crosslinking, while also possessing intrinsic bioactivity and metabolically active degradation products

[25-27]. FTIR and *in vitro* release studies confirmed that SF@LA-NPs remain stable under biological conditions but undergo rapid drug release in a reductive environment with elevated GSH levels, mimicking the intracellular tumor milieu. This aligns with the design principles of stimuli-responsive drug delivery systems and offers the advantage of being triggered by internal physiological signals, thereby avoiding the need for external activation and improving translational feasibility [28, 29]. Notably, SF@LA-NPs also exhibited moderate pH sensitivity, with a higher release rate observed at pH 5.5 compared to pH 7.4. This phenomenon may be attributed to two factors: first, the acidic environment may affect the dynamic equilibrium of disulfide bond exchange reactions within the LA-based nanoparticles, leading to partial destabilization; second, the solubility and diffusion coefficient of SF may increase under acidic conditions, thereby promoting passive diffusion-driven release. This property may facilitate drug release from the nanoparticles in the acidic tumor microenvironment or within intracellular endo/lysosomal compartments, complementing the GSH-triggered release mechanism. Comprehensive physicochemical characterization revealed that SF@LA-NPs possess a uniform size distribution, favorable dispersion, and high encapsulation rate (85.4%), with a drug loading capacity of 14.9%. Importantly, cellular uptake assays demonstrated that SF@LA-NPs increased intracellular delivery efficiency by approximately 6.5-fold. This provides a mechanistic explanation for the significantly improved *in vitro* anti-tumor effect of SF@LA-NPs (IC_{50}: 46 μM), which was markedly lower than that of free SF (IC_{50}: 182 μM), highlighting the essential role of nanoscale transport [30].

Building upon the enhanced delivery efficiency, this study further elucidates the complex mechanisms by which SF@LA-NPs induce cell death beyond simple intracellular drug accumulation. Our results support a hierarchical signaling cascade in which SF@LA-NPs markedly increase intracellular ROS, leading to mitochondrial damage, manifested as a loss of membrane potential, an increased Bax/Bcl-2 ratio, and release of cytochrome c into the cytosol, ultimately activating the classic Caspase-3/PARP-dependent apoptotic pathway. Importantly, these effects were substantially attenuated by the antioxidant NAC, establishing that ROS acts as a critical upstream trigger in this process. Notably, the magnitude of ROS generation induced by SF@LA-NPs far exceeded that of free SF, indicating that the LA-based nanocarrier actively participates in redox regulation. This observation supports the emerging concept of "carrier-drug synergy", in which the carrier itself contributes to therapeutic efficacy [31].

This study also observed that SF@LA-NPs simultaneously induced a protective autophagic response, revealing a dynamic interplay between autophagy and apoptosis. Pharmacologic inhibition of autophagy using 3-MA effectively reduced autophagy-associated markers, including LC3-II conversion and p62 degradation, while enhancing apoptotic signaling and cytotoxicity. Conversely, inhibition of apoptosis using Z-VAD-FMK reduced cytotoxicity but was accompanied by an increase in autophagy-related indicators. These findings suggest that tumor cells activate cytoprotective autophagy as an adaptive defense mechanism against the pro-apoptotic effect induced by SF@LA-NPs. This observation is in line with previous reports describing the bidirectional regulatory effects of SF on autophagy [9, 32], and more importantly, provides mechanistic support for combination therapy that integrates nanomedicine with autophagy inhibition. Of note, while this study assessed autophagic flux primarily through LC3-II conversion and p62 degradation, we further conducted time-course analysis (6 h, 12 h, 24 h), showing that the LC3-II/I ratio peaked at 12 h and declined at 24 h while p62 levels continuously decreased. This dynamic pattern is indicative of active autophagic flux rather than mere autophagosome accumulation. Additionally, treatment with 3-MA, an inhibitor of autophagy initiation, significantly reduced LC3 puncta formation and partially reversed cytotoxicity, functionally corroborating the involvement of autophagy.

This study remains at the preclinical, in vitro stage and has certain limitations. First, the cellular experiments were conducted using only a single U87-MG cell line. Given the high heterogeneity of glioblastoma, different cell lines exhibit significant variations in genetic background, drug sensitivity, and signaling pathway activity. Consequently, results obtained from a single cell line may not fully capture the biological characteristics of glioblastoma. Although U87-MG is one of the most widely used glioma cell lines, further validation in additional models, such as U251, T98G, and LN229, is necessary to improve the generalizability and reliability of the conclusions. Second, *in vitro* cellular models cannot fully recapitulate the complexity of the *in vivo* tumor microenvironment or critical physiologic barriers such as the BBB. Therefore, the *in vivo* targeting efficiency, biodistribution, and BBB penetration capability of SF@LA-NPs require systematic validation in appropriate animal models. In addition, the long-term safety profile of SF@LA-NPs, including potential accumulation toxicity, immunogenicity, and metabolic clearance, warrants further evaluation. Third, although this study identified a functional antagonism between protective autophagy and apoptosis, the molecular regulators governing their crosstalk (e.g., p53 and Beclin-1) have not yet been elucidated. Fourth, with respect to autophagic flux assessment, classical lysosomal inhibitors such as chloroquine were not employed to directly demonstrate LC3-II accumulation upon flux blockade. Although the present time-course analysis and 3-MA experiments strongly support enhanced autophagic flux, the lack of chloroquine-based validation represents a methodological limitation. Future studies incorporating such approaches will provide more rigorous evidence. Finally, based on the mechanistic findings of this study, the combined therapeutic strategy of SF@LA-NPs with autophagy inhibitors may represent a promising therapeutic direction. However, their efficacy and safety must be systematically validated in orthotopic glioblastoma animal models. These efforts will be essential for advancing this nanoplatform toward potential clinical application.

Conclusion

This study successfully developed a redox-responsive nano-delivery system, SF@LA-NPs, based on the endogenous compound (R)-(+)-lipoic acid to enhance the therapeutic performance of SF. Mechanistically, SF@LA-NPs induce excessive ROS generation, leading to mitochondrial dysfunction and simultaneous activation of cytoprotective autophagy. The antagonistic interplay between apoptosis and autophagy suggests that inhibition of autophagy can promote apoptosis and cell death, while inhibition of apoptosis attenuates therapeutic efficacy and may upregulate autophagy. This indicates that the protective autophagy induced by SF@LA-NPs themselves is a pharmacologically modifiable target of drugs that have developed resistance. Overall, this study provides a promising nanoplatform and mechanistic basis for combination strategies integrating nanomedicine with autophagy modulation in glioblastoma treatment.

Acknowledgements

This study was supported by the Guizhou Provincial Basic Research Program (Natural Science, Nos. ZK[2022] 674).

Disclosure of conflict of interest

None.

Address correspondence to: Xin Dai, Department of Basic Teaching, Zunyi Medical and Pharmaceutical College, No. 8, North Section of Ping'an Avenue, Xinpu New Area, Zunyi 563006, Guizhou, China. E-mail: dxshu0419@163.com

References

[1] Abbaszade Z, Bagca BG and Avci CB. Molecular biological investigation of temozolomide and KC7F2 combination in U87MG glioma cell line. Gene 2021; 776: 145445.

[2] Hausmann D, Hoffmann DC, Venkataramani V, Jung E, Horschitz S, Tetzlaff SK, Jabali A, Hai L, Kessler T, Azoŕin DD, Weil S, Kourtesakis A, Sievers P, Habel A, Breckwoldt MO, Karreman MA, Ratliff M, Messmer JM, Yang Y, Reyhan E, Wendler S, Löb C, Mayer C, Figarella K, Osswald M, Solecki G, Sahm F, Garaschuk O, Kuner T, Koch P, Schlesner M, Wick W and Winkler F. Autonomous rhythmic activity in glioma networks drives brain tumour growth. Nature 2023; 613: 179-186.

[3] Rjeibi I, Mabrouk K, Mosrati H, Berenguer C, Mejdoub H, Villard C, Laffitte D, Bertin D, Ouafik L, Luis J, Elayeb M and Srairi-Abid N. Purification, synthesis and characterization of AaCtx, the first chlorotoxin-like peptide from Androctonus australis scorpion venom. Peptides 2011; 32: 656-663.

[4] Qin H, Luo S, Zuo W, Cao Z, Assaraf YG and Kwok HF. Targeted eradication of glioblastoma via venom decapeptide-conjugated dendrimers: Inducing nuclear translocation and au-

tophagic cell death. J Control Release 2025; 383: 113780.

[5] Amin A, Gali-Muhtasib H, Ocker M and Schneider-Stock R. Overview of major classes of plant-derived anticancer drugs. Int J Biomed Sci 2009; 5: 1-11.

[6] Serviddio G, Bellanti F, Stanca E, Lunetti P, Blonda M, Tamborra R, Siculella L, Vendemiale G, Capobianco L and Giudetti AM. Silybin exerts antioxidant effects and induces mitochondrial biogenesis in liver of rat with secondary biliary cirrhosis. Free Radic Biol Med 2014; 73: 117-126.

[7] Bai ZL, Tay V, Guo SZ, Ren J and Shu MG. Silibinin induced human glioblastoma cell apoptosis concomitant with autophagy through simultaneous inhibition of mTOR and YAP. Biomed Res Int 2018; 2018: 6165192.

[8] Kim SH, Choo GS, Yoo ES, Woo JS, Lee JH, Han SH, Jung SH, Kim HJ and Jung JY. Silymarin inhibits proliferation of human breast cancer cells via regulation of the MAPK signaling pathway and induction of apoptosis. Oncol Lett 2021; 21: 492.

[9] Wang C, He C, Lu S, Wang X, Wang L, Liang S, Wang X, Piao M, Cui J, Chi G and Ge P. Autophagy activated by silibinin contributes to glioma cell death via induction of oxidative stress-mediated BNIP3-dependent nuclear translocation of AIF. Cell Death Dis 2020; 11: 630.

[10] Rathore P, Arora I, Rastogi S, Akhtar M, Singh S and Samim M. Collagen nanoparticle-mediated brain silymarin delivery: an approach for treating cerebral ischemia and reperfusion-induced brain injury. Front Neurosci 2020; 14: 538404.

[11] Ashique S, Mohanto S, Kumar N, Nag S, Mishra A, Biswas A, Rihan M, Srivastava S, Bhowmick M and Taghizadeh-Hesary F. Unlocking the possibilities of therapeutic potential of silymarin and silibinin against neurodegenerative diseases-a mechanistic overview. Eur J Pharmacol 2024; 981: 176906.

[12] Kheraldine H, Rachid O, Habib AM, Al Moustafa AE, Benter IF and Akhtar S. Emerging innate biological properties of nano-drug delivery systems: a focus on PAMAM dendrimers and their clinical potential. Adv Drug Deliv Rev 2021; 178: 113908.

[13] Abdellatif AA, Mohammed HA, Khan RA, Singh V, Bouazzaoui A, Yusuf M, Akhtar N, Khan M, Al-Subaiyel A and Mohammed SA. Nano-scale delivery: a comprehensive review of nanostructured devices, preparative techniques, site-specificity designs, biomedical applications, commercial products, and references to safety, cellular uptake, and organ toxicity. Nanotechnology Reviews 2021; 10: 1493-1559.

[14] Yu F, Zhang G, Sun J, Zhao Y, Qi Y, Han X, Ai C, Sun W, Duan J and Yu D. Nanotension relief agent enhances tissue penetration by reducing solid stress in pancreatic ductal adenocarcinoma via Rho/ROCK pathway inhibition. Biomater Res 2025; 29: 0173.

[15] Tu L, Chen S, Yuan Z, Xiong Y, Luo B, Chen Y, Hou Z, Ke S, Lin N, Li C and Ye S. Amino acid-based metallo-supramolecular nanoassemblies capable of regulating cellular redox homeostasis for tumoricidal chemo-/photo-/catalytic combination therapy. J Colloid Interface Sci 2024; 663: 810-824.

[16] Mondal A, Das S, Ali SM, Kolay S, Sengupta A and Molla MR. Bioderived lipoic acid-based dynamic covalent nanonetworks of poly(disulfide)s: enhanced encapsulation stability and cancer cell-selective delivery of drugs. Bioconjug Chem 2023; 34: 489-500.

[17] Xue X, Li C, Yu X, Chenchai K, Zhang X, Zhang X, Zhang G and Zhang D. Photo-patternable and healable polymer semiconductor enabled by dynamic covalent disulfide bonding. Angew Chem Int Ed Engl 2025; 64: e202425172.

[18] Dai L, Liu J, Yang T, Yu X, Lu Y, Pan L, Zhou S, Shu D, Liu Y, Mao W and Qian Z. Lipoic acid-boronophenylalanine-derived multifunctional vesicles for cancer chemoradiotherapy. Nat Commun 2025; 16: 1329.

[19] Liao C, Dai X, Chen Y, Liu J, Yao Y and Zhang S. Biogenic (R)-(+)-lipoic acid only constructed cross-linked vesicles with synergistic anticancer potency. Adv Funct Mater 2019; 29: 1806567.

[20] Cui R, Li B, Liao C and Zhang S. Copper-mediated chemodynamic therapy with ultra-low copper consumption by doping cupric ion on cross-linked (R)-(+)-lipoic acid nanoparticles. Regen Biomater 2023; 10: rbad021.

[21] Yang F, Chen Y, Zhang J, Liao C and Zhang S. Cross-linked (R)-(+)-lipoic acid nanoparticles with prodrug loading for synergistic cancer therapy. J Mater Chem B 2021; 9: 1583-1591.

[22] Wang J, Xie J, Liu Y, Ding R, Mu S, Wang D and Li J. Metal-based nanomaterials achieve tumor treatment strategies by overcoming the blood-brain barrier of glioma and responding to the tumor microenvironment. Mater Today Bio 2025; 36: 102735.

[23] Lim M, Xia Y, Bettegowda C and Weller M. Current state of immunotherapy for glioblastoma. Nat Rev Clin Oncol 2018; 15: 422-442.

[24] Tan J, Duan X, Zhang F, Ban X, Mao J, Cao M, Han S, Shuai X and Shen J. Theranostic nanomedicine for synergistic chemodynamic therapy and chemotherapy of orthotopic glioma. Adv Sci (Weinh) 2020; 7: 2003036.

[25] Yin N, Wang B, Wang Y, Tian L, Han S, Zheng B, Feng F, Song S and Zhang H. A metal-phenolic network nanoresensitizer overcoming glioblastoma drug resistance through the metabolic adaptive strategy and targeting drug-tolerant cells. Nano Lett 2025; 25: 9570-9580.

[26] Bossio S, Perri A, Gallo R, De Bartolo A, Rago V, La Russa D, Di Dio M, La Vignera S, Calogero AE, Vitale G and Aversa A. Alpha-lipoic acid reduces cell growth, inhibits autophagy, and counteracts prostate cancer cell migration and invasion: evidence from in vitro studies. Int J Mol Sci 2023; 24: 17111.

[27] Pibiri M, Sulas P, Camboni T, Leoni VP and Simbula G. α-lipoic acid induces endoplasmic reticulum stress-mediated apoptosis in hepatoma cells. Sci Rep 2020; 10: 7139.

[28] Jia Y, Wu Y, Zhang F, Sun Y and Liu Y. Overcoming the blood-brain barrier challenge: nanotechnology-enhanced photodynamic therapy for glioblastoma treatment. Chem Commun (Camb) 2025; 61: 12431-12448.

[29] Zha S, Liu H, Li H, Li H, Wong KL and All AH. Functionalized nanomaterials capable of crossing the blood-brain barrier. ACS Nano 2024; 18: 1820-1845.

[30] Perini G, Giulimondi F, Palmieri V, Augello A, Digiacomo L, Quagliarini E, Pozzi D, Papi M and Caracciolo G. Inhibiting the growth of 3D brain cancer models with bio-coronated liposomal temozolomide. Pharmaceutics 2021; 13: 378.

[31] Hou J, Hao L, Du W, Su Q, Xiong Q, Zhao W and Yang Z. α-lipoic acid nanoparticles functionalized with RVG29 peptide attenuate seizure-induced neurotoxicity by restoring mitochondrial homeostasis via the PINK1/Parkin pathway. Free Radic Biol Med 2026; 245: 201-222.

[32] Duan WJ, Li QS, Xia MY, Tashiro S, Onodera S and Ikejima T. Silibinin activated ROS-p38-NF-κB positive feedback and induced autophagic death in human fibrosarcoma HT1080 cells. J Asian Nat Prod Res 2011; 13: 27-35.